Quantifying embolism: label free volumetric mapping of thrombus structure and kinesis in a microfluidic system with optical holography

Xuefei He,[a] Samantha J. Montague,[a,b] , Xu Tao [a], Elizabeth E. Gardiner,[b] Woei Ming Lee [a,b*]

[a] Research School of Engineering, College of Engineering and Computer Science, The Australian National University, Canberra ACT 2601, Australia

[b] ACRF Department of Cancer Biology and Therapeutics, John Curtin School of Medical Research, The Australian National University, Canberra ACT 2601, Australia

Address for correspondence
Dr W M Lee
Research School of Engineering,
College of Engineering and Computer Science,
The Australian National University,
Canberra ACT 2601, Australia
*Email: steve.lee@anu.edu.au

Key words: platelet, thrombus, adhesion receptors, quantitative phase microscopy

Key points

1. **Label- free imaging of a developing thrombus**
2. **Holographic QPM Imaging for real time volume quantification**
3. **Growth, contraction and stability of a thrombus formed on a microfluidic chip.**
4. **In vitro studies of embolization**

Abstract

Embolization of thrombotic material may lead to acute events such as ischaemia and myocardial infarction. The embolus is the physical detachment from a primary thrombus that has developed under fluid shear rates. The physical characteristics (surface area coverage, volume, mass and packing density) of a thrombus influence the overall flow dynamics of an occluding blood vessel. Here, we demonstrate the effectiveness of holographic quantitative phase microscopy (QPM) in identifying multiple morphological parameters of a thrombus (volume, surface area and height) formed over collagen-coated microfluidic channels by exerting a range of shear rates with anticoagulated platelet-rich plasma (PRP) and whole blood. QPM enables the recording of entire thrombus volumes in real-time using PRP and observed both growth and contraction trends of thrombi, without need for biochemical labelling. We quantified the process of emboli detachment in a microfluidic channel under pathophysiological shear rates (7500 s^{-1}, 12500 s^{-1}). Rapid and direct quantification of an embolizing thrombus can enable the study of events during undesirable vessel occlusion and lead to targeting and early diagnosis of acute coronary and venous events.

Introduction

Platelets are specialized anucleate blood cells that are essential for maintaining hemostasis. Hemostasis, the process of maintaining a normal blood volume, which often involves the forming of a blood clot (thrombus). Thrombus formation is initiated by adhesion of circulating blood platelets onto exposed extracellular matrix proteins, including collagen and von Willebrand Factor (VWF), within a damaged vascular wall. Adhered platelets then release secondary agonists/mediators and promote thrombin generation, which helps recruit additional platelets to the injured site, cumulatively building a thrombus. Under pathophysiological conditions, this normally protective cascade of events can result in arterial thrombosis or deep vein thrombosis, which can be responsible for major clinical events such as heart attack and stroke.

Real time monitoring of thrombus formation under fluidic settings is vital for studying the thrombotic process and provides significant insight to studying dynamic platelet function [1, 2]. Studying the initial molecular events as a thrombus develops are crucial to understanding the involvement of key platelet receptors and can also help in assessing platelet dysfunction in patients with genetic defects [2]. Measuring the growth of a thrombus would be useful in identifying targets to reduce pathophysiological events such as arterial thrombosis. Finally, the ability to study thrombus stability at pathological shear rates will inform on molecular processes involved in embolization, and facilitate the development of therapeutic avenues to treat venous thrombosis.

A developing thrombus can be classified into a series of morphological transitions along a high fluid shear. The transition starts off with the initial activation of platelets through engagement of platelet signalling receptors which trigger activation of platelet integrin receptors and drive the aggregation of platelets that leads to thrombus growth before undergoing contraction [3, 4]. The contractile forces [5] from the platelet are in part due to the interaction with the surrounding fibrin network [6]. On top of that, the degree of activation of each platelet in the thrombus influences how the platelets engage each other; fully

activated platelets are held together within the thrombus by fibrinogen binding and bridging adjacent integrin αIIbβ3 receptors. Over time, adherent and fully activated platelets form the stable core of a thrombus, and newly-arrived, less-activated platelets are more loosely packed and held together forming a shell-like zone. The molecular composition of the thrombus core and shell affect the overall structural stability of the thrombus [7]. To understand the basic biological processes underpinning thrombus growth and regulation of that growth, it is important to visualize the morphological development of a thrombus in real time using high speed imaging instruments that directly capture multiple views of a single thrombus and quantitates parameters including volume, height and area, simultaneously and temporally.

Fluorescence intensity emitted from platelet-targeted fluorescent probes and surface markers are used to map out the overall architecture of thrombus [8, 9]. The two main fluorescence imaging methods are wide field fluorescence microscopy (WFM) and confocal laser scanning microscopy (CLSM) [10] . In WFM, the changes of fluorescence intensity over a given area are used to estimate the volume of the thrombus. The advantage of WFM imaging is the speed of acquisition, which is limited by the frame rate of the imaging camera and also the brightness of the fluorescence signals. The fluorescence signal collected on a digital imaging camera is integrated from a single imaging focal depth of around 8 μm (based on objective of magnification 10x and NA 0.25) [11-13]. This means that the capacity to measure the thickness of thrombus is restricted by the focal depth of the imaging lenses used. Therefore, if a thrombus is larger than the focal depth, the quantification would encounter inaccuracies in volume quantification [14, 15] . To circumvent this, most researchers have turned to more precise CLSM imaging that captures the whole thrombus through multiple two dimensional thin imaging slices recorded by raster scanning at a focused laser spot. This technique offers more accurate depth and thickness quantification along with area and density of a thrombus [2, 16, 17]. The full 3D images acquired from CLSM imaging requires repeated scanning of a laser beam across the sample through mechanical devices such as galvanometer mirrors [2, 16, 17] of around 2 Hz at full frame or by spinning disc [18] that can reach 1000 Hz.

The scanning process also exposes sample to higher light irradiation that can result in photobleaching [19] or photodamage [20]. In fluorescence imaging, there is an additional complication introduced by binding fluorescently-conjugated antibodies to the platelet surface to provide specificity. Recently, quantitative phase microscopy (QPM) techniques have provided new opportunities to measure thrombus formation *in vitro* [21]. QPM maps out the difference in refractive index instead of using endogenous fluorescence signal and records thickness of the sample directly. However, since refractive index differences in biological samples are non-specific, this quantification tool requires a careful choice of biological samples [22, 23].

QPM is usually in two forms, non-holographic and holographic type. The non-holographic QPM [23] combines existing imaging optics of a WFM with numerical phase calculation and a prior knowledge to estimate the phase (refractive index difference) before it can generate a reconstructed volume of the sample. Although it has the same optical limitation as a conventional WFM, it provides volumetric quantification that is not available in conventional WFM, albeit at the low imaging speed. Holographic QPM [24-26], on the other hand, directly records the phase of the object and uses a non-focussed laser light. This method is not limited by the focal depth of the imaging optics in WFM or a focus laser beam in CLSM. The recorded phase also removes undesired optical distortion arising from any artefact or deformation within the sample [27, 28] which is important especially when dealing with samples of high scattering signals such as blood samples. Recently, Boudejltia and colleagues [29-31] showed that QPM can quantify individual platelet adhesion and other groups [32] have also began to using non-holographic QPM techniques to quantify the mass of the final thrombus. All in all, the application of QPM techniques in platelet and thrombus studies is in their infancy because of the lack of physiological relevant outcomes. We argue that QPM is uniquely positioned to present comprehensive and direct multi-dimensional morphological information of a developing thrombus, which would not be straightforward in other imaging modalities.

Table 1 and Figure 1 present the three imaging modalities; WFM, CLSM and QPM that are typically used to quantify thrombus. Table 1 lists out the performances of the three modalities. Figure 1a) illustrates the dynamic growth of a thrombus under flow at different time points (t_1 to t_3). Figure 1b) shows how WFM imaging captures the integrated fluorescence over a given thrombus. Figure 1c) illustrates the multiple thin image slices (Z_0 to Z_n) that depict recorded fluorescence intensities at each slice, $I(z_i)$, from which CLSM retrieves the thrombus volume. The repeated scanning of a highly focused laser beam causes an ineluctable lag time of round trip scanning which increases the overall acquisition time. Figure 1d) shows how QPM imaging methods directly measure the refractive index difference of the thrombus which is directly translated to integrated volume. Another advantage in QPM is that the volume does not depend on the brightness emitted from the sample or the dynamic range of the detector as compared to WFM.

By demonstrating that QPM can measure dynamic events and parameters such as volume, height and area simultaneously and temporally at the different stages of thrombus formation and at multiple viewing points, this will enable a high throughput morphological mapping of thrombus development and greatly accelerate the understanding of early stages of thrombus development in a flow assay. A well developed and robust imaging framework using holographic QPM techniques also lends itself to on-chip holographic imaging techniques that be directly applied to diagnosing disorders of platelet function [33, 34].

Results

We used platelet-rich plasma (PRP) in a microfluidic environment to obtain optical holograms of thrombus formation (in this context, platelet-platelet aggregates formed through platelet deposition on to collagen), which were digitally recorded on a high speed digital camera [35]. We used automated image processing [36] for rapid quantification of individual thrombi over a given field of view. Within a single acquisition, we directly generate multi-parameter datasets including thrombus volume, height and surface

area. Since optical holograms record all volumetric information in a single snapshot, there is no requirement to actively change the focus position of the imaging lenses. As the holograms are essentially 2D images, it enables directly volumetric imaging and the speed is limited only by the camera frame rate (150 fps). Figure 2 shows the diagram of holographic QPM imaging and microfluidic setup. In Figure 2a) i) and ii) shows the actual microfluidic chips and the corresponding cross-sectional sketch respectively. Figure 2a) iii) depicts the position of the imaging microscopy objective (MO) that is placed under the microfluidic chip to collect the exiting laser light through the sample. The exiting laser light is recombined with a reference laser light at a CCD camera –using a beam splitter. The interference pattern of the two laser light fields creates the optical hologram. A syringe pump was used in suction mode to draw the sample; either whole blood (with heparin (10 U/mL) or 3.2% tri-sodium citrate used as an anticoagulant) or platelet-rich plasma (PRP), collected from heparinized or citrated blood, across a collagen-coated microfluidic chip surface, minimizing unnecessary sample shear stress prior to entry into the microfluidic slide. The direction of flow is represented by the arrows (Figure 2a). Due to difference in flow margination between platelet rich plasma (PRP) and whole blood, different regions within the flow channel are more prone to aggregation. For example, aggregates from PRP formed close to edges of the channel whereas aggregates in whole blood tended to form in the middle of the channel. To ensure fair comparison, we selected thrombi that were formed within defined regions 100 µm from the channel side walls. Additional information of the sample and microfluidic chip preparations is discussed in the experimental section.

- **From growth to reduction**

During thrombus formation, the different levels of activation of the platelets contribute to the overall packing density which affects physical stability of the adhering thrombus. During the initial stage of thrombus formation, there is a steady increase in volume which is followed by an overall thrombus

consolidation/contraction [37]. During physiological thrombus formation where fibrin is generated, the thrombus contraction is mediated in part by activated platelets pulling on fibrin networks to form a closely packed core [38]. The morphological change in the thrombus is orchestrated by mechanical and biochemical cues received by a formed thrombus. It has been showed that rate of diffusion of agonist within the thrombus is regulated by how platelets are packed [39]. The anticoagulated blood used in this work to generate thrombi refers to the quantification of platelet deposition and platelet-platelet aggregation and that the process of fibrin generation was not studied.

To investigate the morphological changes in thrombus formation, we perfused PRP over collagen-coated microfluidic channels at three different flow rates that produce fluid shear rates that are physiological relevant to thrombus formation at 72 µL/min (1800 s^{-1} shear rate; 18 dyne/cm^2 shear stress), 144 µL/min (3600 s^{-1} shear rate; 36 dyne/cm^2 shear stress) and 288 µL/min (7200 s^{-1} shear rate; 72 dyne/cm^2 shear stress) for 10 min. To investigate the parameters of thrombi formed under flow of whole blood, we perfused heparinized whole blood over collagen–coated microfluidic channels for 10 min at two different flow rates, with equivalent shear stress to PRP samples, 32 µL/min (800 s^{-1} shear rate; 36 dyne/cm^2 shear stress) and 72 µL/min (1600 s^{-1} shear rate; 72 dyne/cm^2 shear stress). The detailed conversion of shear stress, shear rate and flow rate can be found in Experimental section. The field of view for capturing dynamic thrombus formation was fixed on sections close to the inlet within ~ 800 ±200 µm after the inlet, for all the measurements to ensure consistency and minimal exposure to turbulent flow. Volumetric information was later reconstructed through classical holographic numerical approaches (see Experimental section). Figure 2 b) i) shows the result of the volumetric changes of thrombus formed at three different fluidic shear rates using PRP collected from heparinized blood from a single donor (d1). The x-coordinate indicates time in second and y-coordinate is for the volume in cubic micrometre. The blue, yellow and red lines indicate the thrombus formed under the 1800 s^{-1}, 3600 s^{-1} and 7200 s^{-1} shear rates respectively. Detailed statistic methods can be found in Experimental section. Figure 2 b) ii) shows

the height map for each thrombus in Figure 2 b) i) at different time points. The scale bar is 30 μm and the colour bar indicates the height in micrometres. The growth trends shown in Figure 2 b) present a linear growth followed by plateau, which is similar with previously reported growth trends [38] and mostly similar shape to growth trends of citrated PRP (Supplementary Figure A2) . To quantify the growth rate, two linear fits (R-square above 0.9) were applied to the growth and plateau segments respectively, marked by black lines and S_1 and S_2. S_1 represents the speed of the volume accumulation before the maximum point. S_2 represents the speed volume reduction after the maximum point. The statistics average of growth rate S_1 (the positive Y axis) and reduction rate S_2 (the negative Y axis) from all donors are presented in Figure 2 c) ii). The influence of the shear rate appears to be more dominant at 7200 s^{-1} compared with shear rates of 1800 s^{-1} and 3600 s^{-1}. While higher shear rates seem to suggest a rapid ascent, the speed (S_2) of the decline appears to be small (< 1200 μm^3/min) for all the thrombi formed at three different shear rates, which is likely to be related to platelet contraction [39, 40] under flow. The quantitative observation of the events is made possible because of the robustness of holographic QPM sensitivity.

- **Characteristics of individual thrombus**

After the 10 min formation process, we changed the flowing PRP or whole blood sample to the buffer (physiological saline; 0.9% NaCl) at the same shear rate previously used to remove excess PRP or whole blood and then translated the imaging field of view throughout the whole channel to capture images of individual thrombi. Using holographic QPM, we retrieved thrombus volume, surface area and maximum height after numerical reconstruction (see Experimental section) as shown in Figure 3. Figure 3 a) shows a perspective view of a reconstructed thrombus formed by PRP and whole blood. Figure 3 b) and c) show the measured volumes, surface areas and peak heights of thrombi formed by PRP and whole blood respectively. Each data point in the figure represents individual thrombi formed at different fluid shear (1800 s^{-1}, 3600 s^{-1}, 7200 s^{-1}). Differences were observed between thrombi generated with heparinized

PRP and citrated PRP. The thrombi volumes appeared to be greater for citrated PRP thrombi that could be attributed to the increased in height without a significant increase in area of under which platelet is adhering to. The distribution of the thrombus peak height is presented in the Supplementary material Fig. A1. Within the microfluidic system the thrombus height (heparin PRP and citrated PRP) ranged from 1.43 µm to 34.37 µm with median of 8.114 µm ± SD = 4.933. We observed that the volume and area of the individual thrombi from all the donors displayed significant degrees of variation. Hence, it would be of great interest to couple signatures between molecular and morphological information from each thrombus in future studies. However, this would require the combination of fluorescence imaging with holographic QPM [41] to give further information. By using the abundant characteristics information of individual thrombus morphology, it would be very informative to test functionality of platelets by controlled variables such as surface density of platelet receptors which control onset of platelet adhesion and thrombus formation. The phase images retrieved from digital holographic microscopy (DHM) provide the morphological information that is usually examined in platelet study using WFM or CLSM at the same temporal resolution. In addition to that, the morphological information would help developed a better thrombotic numerical model [42].

- **Quantifying embolism**

The spontaneous embolism of a thrombus especially in acute coronary events may be a natural protective mechanism against infarction in organs [43]. Past studies have focused on individual platelet behaviour and more recently, there has been new interest in investigating factors related to thrombus stability that are able to be correlated with acute coronary events. Here, we investigate overall thrombus stability by perfusing a buffer at a high shear rate over a formed thrombus for a certain period of time and monitored thrombus parameters. The stability test could provide a new perspective to investigate the inner core and the outer shell regions of thrombus [44]. Figure 4 a) illustrates the experiment undertaken where a

thrombus that was previously formed with shear rates of either 1800 s^{-1}, 3600 s^{-1} and 7200 s^{-1} with PRP or at 800 s^{-1}, 1600 s^{-1} with whole blood is then exposed to an additional saline buffer at a shear rate of 7500 s^{-1} for 5 minutes and 12500 s^{-1} for 2 minutes. To ensure a fair comparison of the volume, we selected aggregates with equivalent surface areas (1000 - 1800 μm^2) and similar distance (~ 800 ±200 µm) from the channel inlet. Structural change during the flush could reflect the stability of the thrombus formed. Figure 4 shows the stability test results. Figure 4 b) i) shows an example of the change in volume for three individual thrombi (pre-formed by 1800 s^{-1}, 3600 s^{-1} and 7200 s^{-1} shear rate, heparin PRP) from donor 4 (d4) during the stability test. Figure 4 c) i) shows the change in volume for thrombus pre-formed by 800 s^{-1}, 1600 s^{-1} shear rate (equivalent shear stress as medium and high PRP shear rates) with heparinized whole blood from donor 4 during the stability test. The corresponding volumetric images are displayed in Figure 4 b) ii) and 4 c) ii). Figure 4 b) iii), iv) and v) as well as Figure c) iii), iv) and v) show the volume, surface area and height before and after the test. Each dot (circle for a thrombus formed under 1800 s^{-1}, triangle for 3600 s^{-1}, square for 7200 s^{-1}) in the bar represents the average data (obtained from n>8 data points) from each donor (D2, D3, D4 for citrated PRP, four donors for heparin PRP (d1-4) and four donors for heparinized whole blood). The statistical test performed was a paired t-test and significance was observed when $p<0.05$. There was decreased volume post-perfusion with citrate PRP at 3600 s^{-1} (*$p<0.05$), due to a reduction in thrombus height (*$p<0.05$; Figure 4b) iii and v). Reduction in height was also observed at the same shear rate with heparin PRP, although there was no significant reduction in volume. The rapid decrease in volume with citrated PRP suggests an unstable outer thrombus layer that breaks apart with a residual core thrombus remaining in the same site. This leaves a thrombus of smaller volume and height. However, the surface area of the thrombus is maintained relatively, except for thrombi formed by heparin PRP at 3600 s^{-1}. In addition, the thrombus formed at lower shear rates (1800 s^{-1} and 3600 s^{-1}) retains a volume, area and height that are smaller than the

thrombus formed at 7200 s^{-1}. We showed that holographic QPM can rapidly track, capture and quantify the rich dynamics of a developing thrombus.

Discussion

We have shown that the application of holographic QPM provides multi-parameter classification of morphological information in real time. Since depth of focus of the imaging system of QPM is not restricted, QPM retrieves the entire morphological information set of a developing thrombus without any form of labelling. Without QPM, it would require considerable sample preparation and imaging time to retrieve the morphological information. Furthermore, whole blood presents a challenge in optical imaging as red blood cells (RBC) scatter light in a highly directional and ballistic manner, Mie scattering [45]. By combining advanced digital signal processing techniques with digital optical holography this enables the removal of optical scattering and increase imaging resolution. With deterministic microfluidic parameters, the ballistic scattering property of RBC could be removed. We have previously shown that incremental thresholding allows one to retrieve images of an object embedded in a scattering medium [36]. Further, Ferraro and colleagues have demonstrated the use of multi-frame holographic imaging to retrieve images of objects from flowing blood that are "hidden" [46, 47]. However, imaging through turbid or scattered medium remains a major imaging challenge, with holographic microscopy being a key technique [48, 49]. Many more recent techniques in optical holography [47-50] can be applied to the analysis of thrombus formation in whole blood. However, one main limitation in the application of QPM is the non-specificity of the imaging technique that does not offer additional molecular information i.e. surface receptor levels. To achieve both morphological and molecular imaging, there is a need to combine QPM and high speed fluorescence imaging techniques such as lightsheet microscopy [1]. This provides a greater insight into the dynamic interaction of different receptors and adhesion molecules to thrombus formation. While high speed fluorescence microscopy requires specialized imaging sensors, holographic QPM can operate with more general imaging sensors [51]. Hence, it is plausible to incorporate

holographic QPM and microfluidic systems into a single portable unit. By reducing the footprint of holographic QPM and using unlabeled samples, it would be possible to use such a compact optofluidic system [52] to directly quantify dynamic thrombus morphology in a clinical setting. Here, we have used a limited number of healthy donors, which would need to be increased to permit comparative studies of thrombus growth rate with a wider distribution of shear rates. This will more accurately portray trends in volumetric growth and reduction over a wider distribution of shear rates. After which, from the clinical perspective, such a system may be effective in testing anticoagulation therapy, identifying platelet dysfunction and monitoring pro-thrombotic stages.

Experimental Section

Blood collection

Venous whole blood was collected from consenting, healthy drug-free volunteers into syringes containing 3.2% trisodium citrate or 10 U/mL heparin (Sigma) as an anticoagulant. Ethical approval was granted by the Australian National University Human Research Ethics Committee (2016/317). Whole blood was supplemented with 40 µM PPACK (D-Phenylalanyl-prolyl-arginine Chloromethyl Ketone; Cayman Chemicals) 5 min before experimental procedure.

Platelet-rich plasma (PRP) was prepared from anticoagulated whole blood by centrifugation at 200 *g* for 20 min and the upper PRP phase was collected. Prior to perfusion, blood samples were checked for absence of visible clots.

Microfluidic channel preparation

The microfluidic channel (400 µm wide, 100 µm height and 1.2 cm long) was made of transparent polydimethylsiloxane (PDMS) by soft lithography method [52]. Before the experiment, the entire microfluidic channel was coated with collagen Reagent HORM 100 µg/mL (Takeda, Austria: a suspension of native equine tendon collagen type I) and incubated overnight at 4°C. The collagen was

added through the outlet to ensure that platelets initially contacted collagen from the entry of the channel beyond the inlet. Before the start of the experiment, the channel was washed using a wash buffer (25 mM TRIS HCl, 150 mM NaCl, pH 7.4) perfused at 300 µL/min for 2 min in the opposite direction of experimental flow.

Image and data processing

The phase images were reconstructed from holograms recorded by CCD camera, using automatic numerical methods [53]. The volumetric images were calculated from the phase images according to equations below using Matlab (MATLAB R2017a). The standardization of the phase measurement were performed with the 3 µm and 50 µm polystyrene microspheres (Polybead® Microspheres, polysciences, Inc.). The detail of the standardization can be found in Supplementary materials. In the equations, x and y are the coordinate of the image, representing each pixel. The $\mathrm{Phase}(x,y)$ is the phase image and the height (x,y) is the volumetric image. The λ is the wavelength of the laser, which is 632.8 nm in our system. The $n_{pt} = 1.399$ and $n_{pa} = 1.332$ are the refractive indexes of platelet and the buffer respectively [37].

Individual thrombus image ($\mathrm{where}\ x,y \in T$) is selected from full field image by Otsu's threshold method [32, 54, 55]. The thrombus characteristics evaluated were thrombus peak height, surface area and volume. The thrombus peak height H is the highest point across an individual thrombus image. The thrombus surface area $S_{thrombus}$ is calculated from the summation of pixels covering the thrombus. The S_p is the actual size of one pixel represents. The value of S_p is calibrated through a 1951 USAF Glass Slide Resolution Target. The volume of thrombus V is calculated by multiplying the number of pixels that the thrombus covered by the volume of each pixel.

$$height(x,y) = -\frac{Phase(x,y) * \lambda}{2\pi * (n_{pt} - n_{pa})}$$

$$H = -maximum[height(x,y)], where\ x,y \in T$$

$$S_{thrombus} = \sum_{x,y} S_p \, , where \; x, y \; \in T$$

$$V = \sum_{x,y} S_p * height(x, y) \, , where \; x, y \; \in T$$

Shear stress conversion

Equation $Q = \frac{Tbh^2}{6\mu}$ is used to calculate the experiment flow rates Q. In the equation, T is the shear stress, b and h are the width and height of the channel, μ is the viscosity of the liquid sample. In our system, channel width is 400 μm, channel height is 100 μm and the viscosity of PRP sample is based on cell culture suspension which is 0.01 $dyne/cm^2 * s$. The viscosity of whole blood sample is 0.045 $dyne/cm^2 * s$.

Statistics

The volume growth data for thrombus formation is first smoothed by a moving average filter (span=50 sampling points, data contains more than 1800 sampling points in total). Then a fitting (polynomial fit with degree of 5 and R-square above 0.98) was applied to each smoothed volume growth line. Two linear fittings (R-square above 0.9) were applied to front and end zone of the polynomial fit, indicated by black lines and the gradient value of the lines are S_1 and S_2 in the unit of cubic micrometre per minute. One set of volume growth data is shown in the Figure 2 b) i) with the two linear fittings (n=1 for each line). All experimental volume growth data can be found in the Supplementary material.

The growth rate shown in the Figure 2 c) ii) are the averaged growth rate from all the experimental data (n=3 for heparin PRP at 1800 s^{-1} and 3600 s^{-1}, n=1 for heparin PRP at 7200 s^{-1}, n=2 for citrated PRP at 1800 s^{-1}, 3600 s^{-1} and 7200 s^{-1}). Software used for data smoothing, fitting and line plots is Matlab (MATLAB R2017a).

The individual thrombus characteristic bar graphs in Figure 3 are shown as means ± SD by One-way ANOVA with Tukey's post-hoc tests and paired t-tests were performed by Graph Pad Prism (version

7) software. Individual scatter dot in the bar graph is representative for each thrombus data. The number of thrombus is marked by n beside each bar. The number of donor is marked by N beside each bar.

The volume, surface area and peak height analysis of stability test in Figure 4 b) iii), iv) and v) and Figure 4 c) iii) iv) and v) are means ± SD by One-way ANOVAs with Tukey's post-hoc tests by Graph Pad Prism software. Each dot represents average data from one donor. The number of donor N= 3 for citrated PRP and N=4 for heparin PRP and whole blood.

Contribution and acknowledgements

WML and EEG conceived the project. XH designed and built the holographic optical microscopy system. TX and XH designed and fabricated microfluidic chip. SJM and EEG designed the platelet experiments. XH and SJM performed the experiments and analysis of the results. All authors interpreted the data and co-wrote the manuscript. We received funding from the National Health and Medical Research Council of Australia and the Australian Research Council. XH is the recipient of the CSC scholarship.

References

[1] T. J. Stalker, E. A. Traxler, J. Wu, K. M. Wannemacher, S. L. Cermignano, R. Voronov, S. L. Diamond, L. F. Brass, *Blood* **2013**, *121*, 1875.

[2] M. Nagy, J. W. Heemskerk, F. Swieringa, *Platelets* **2017**, *28*, 441.

[3] B. Savage, F. Almus-Jacobs, Z. M. Ruggeri, *Cell* **1998**, *94*, 657.

[4] K. Claesson, T. L. Lindahl, L. Faxälv, *Thrombosis and haemostasis* **2016**, *115*, 1178.

[5] V. Tutwiler, H. Wang, R. I. Litvinov, J. W. Weisel, V. B. Shenoy, *Biophysical Journal* **2017**, *112*, 714.

[6] O. V. Kim, R. I. Litvinov, M. S. Alber, J. W. Weisel, *Nature Communications* **2017**, *8*, 1274.

[7] J. D. Welsh, T. J. Stalker, R. Voronov, R. W. Muthard, M. Tomaiuolo, S. L. Diamond, L. F. Brass, *Blood* **2014**, *124*, 1808.

[8] S. Maloney, L. F. Brass, S. Diamond, *Integrative Biology* **2010**, *2*, 183.

[9] K. Neeves, S. Maloney, K. Fong, A. Schmaier, M. Kahn, L. Brass, S. L. Diamond, *Journal of Thrombosis and Haemostasis* **2008**, *6*, 2193.

[10] A. Celi, G. Merrill-Skoloff, P. Gross, S. Falati, D. S. Sim, R. Flaumenhaft, B. C. Furie, B. Furie, *Journal of Thrombosis and Haemostasis* **2003**, *1*, 60.

[11] B. R. Masters, *Journal of Biomedical Optics* **2008**, *13*, 029902.

[12] M. Pluta, P. Maksymilian, *Advanced light microscopy*, Vol. 1, Elsevier Amsterdam, **1988**.

[13] J. B. Pawley, in *Handbook Of Biological Confocal Microscopy*, (Ed: J. B. Pawley), Springer US, Boston, MA **2006**, 20.

[14] J.-A. Conchello, J. W. Lichtman, *Nat Methods* **2005**, *2*, 920.

[15] H. Frost, *Henry Ford Hospital Medical Bulletin* **1962**, *10*, 267.

[16] S. M. De Witt, F. Swieringa, R. Cavill, M. M. Lamers, R. Van Kruchten, T. Mastenbroek, C. Baaten, S. Coort, N. Pugh, A. Schulz, *Nature Communications* **2014**, *5*.

[17] C. Zhang, S. Neelamegham, *Platelets* **2017**, *28*, 434.

[18] W. B. Amos, J. G. White, *Biology of the Cell* **2003**, *95*, 335.

[19] E. Wang, C. M. Babbey, K. W. Dunn, *Journal of Microscopy* **2005**, *218*, 148.

[20] T. Bernas, M. ZarĘBski, R. R. Cook, J. W. Dobrucki, *Journal of Microscopy* **2004**, *215*, 281.

[21] V. Magidson, A. Khodjakov, *Methods in Cell Biology* **2013**, *114*, 10.1016/B978.

[22] V. P. Pandiyan, R. John, *Applied Optics* **2016**, *55*, A54.

[23] K. Lee, K. Kim, J. Jung, J. Heo, S. Cho, S. Lee, G. Chang, Y. Jo, H. Park, Y. Park, *Sensors* **2013**, *13*, 4170.

[24] D. Paganin, K. A. Nugent, *Physical Review Letters* **1998**, *80*, 2586.

[25] M. Arnison, C. Cogswell, N. Smith, P. Fekete, K. Larkin, *Journal of Microscopy* **2000**, *199*, 79.

[26] K. Koos, J. Molnár, L. Kelemen, G. Tamás, P. Horvath, *Scientific Reports* **2016**, *6*, 30420.

[27] C. J. Mann, L. Yu, C.-M. Lo, M. K. Kim, *Optics Express* **2005**, *13*, 8693.

[28] H. Wang, D. Wang, J. Zhao, J. Xie, *Chinese Optics Letters* **2008**, *6*, 165.

[29] T. Colomb, J. KŘhn, F. CharriŔre, C. Depeursinge, P. Marquet, N. Aspert, *Optics Express* **2006**, *14*, 4300.

[30] L. Miccio, D. Alfieri, S. Grilli, P. Ferraro, A. Finizio, L. De Petrocellis, S. Nicola, *Applied physics letters* **2007**, *90*, 041104.

[31] T. Colomb, E. Cuche, F. Charrière, J. Kühn, N. Aspert, F. Montfort, P. Marquet, C. Depeursinge, *Applied Optics* **2006**, *45*, 851.

[32] K. Z. Boudejltia, D. R. de Sousa, P. Uzureau, C. Yourassowsky, D. Perez-Morga, G. Courbebaisse, B. Chopard, F. Dubois, *Biomedical Optics Express* **2015**, *6*, 3556.

[33] S. M. Baker, K. G. Phillips, O. J. McCarty, *Cellular and Molecular Bioengineering* **2012**, *5*, 488.

[34] S. M. Baker-Groberg, K. G. Phillips, O. J. McCarty, *Journal of Biomedical Optics* **2013**, *18*, 016014.

[35] M. Nagy, J. W. M. Heemskerk, F. Swieringa, *Platelets* **2017**, *28*, 441.

[36] A. Onasoga‐Jarvis, T. Puls, S. O'brien, L. Kuang, H. Liang, K. Neeves, *Journal of Thrombosis and Haemostasis* **2014**, *12*, 373.

[37] X. He, C. V. Nguyen, M. Pratap, Y. Zheng, Y. Wang, D. R. Nisbet, R. J. Williams, M. Rug, A. G. Maier, W. M. Lee, *Biomedical Optics Express* **2016**, *7*, 3111.

[38] R. Flaumenhaft, *Blood* **2014**, *124*, 1697.

[39] A. Ono, E. Westein, S. Hsiao, W. S. Nesbitt, J. R. Hamilton, S. M. Schoenwaelder, S. P. Jackson, *Blood* **2008**, *112*, 90.

[40] S. Falati, P. Gross, G. Merrill-Skoloff, B. C. Furie, B. Furie, *Nature Medicine* **2002**, *8*, 1175.

[41] N. Otsu, *Automatica* **1975**, *11*, 23.

[42] S. Chowdhury, J. Izatt, *Opt. Lett.* **2014**, *39*, 1015.

[43] S. Johnson, S. Duffy, G. Gunning, M. Gilvarry, J. McGarry, P. McHugh, *Annals of biomedical engineering* **2017**, *45*, 2494.

[44] D. A. Gorog, Z. A. Fayad, V. Fuster, *Journal of the American College of Cardiology* **2017**, *70*, 2036.

[45] J. M. Steinke, A. P. Shepherd, *Applied Optics* **1988**, *27*, 4027.

[46] V. Bianco, M. Paturzo, A. Finizio, A. Calabuig, B. Javidi, P. Ferraro, *IEEE Journal of Selected Topics in Quantum Electronics* **2014**, *20*, 89.

[47] P. AntonioáNetti, *Lab on a Chip* **2014**, *14*, 2499.

[48] G. Indebetouw, P. Klysubun, *Opt. Lett.* **2000**, *25*, 212.

[49] M. Cui, C. Yang, *Optics Express* **2010**, *18*, 3444.

[50] C.-L. Hsieh, Y. Pu, R. Grange, D. Psaltis, *Optics Express* **2010**, *18*, 12283.

[51] K. M. Dean, P. Roudot, C. R. Reis, E. S. Welf, M. Mettlen, R. Fiolka, *Biophysical Journal* **2016**, *110*, 1456.

[52] Z. S. Ballard, Y. Zhang, A. Ozcan, *Light: Science & Applications* **2017**, *6*, e17105.

[53] Y. Xia, G. M. Whitesides, *Annual Review of Materials Science* **1998**, *28*, 153.

[54] I. V. Kolesnikova, S. V. Potapov, M. A. Yurkin, A. G. Hoekstra, V. P. Maltsev, K. A. Semyanov, *Journal of Quantitative Spectroscopy and Radiative Transfer* **2006**, *102*, 37.

[55] O. Zhernovaya, O. Sydoruk, V. Tuchin, A. Douplik, *Physics in Medicine and Biology* **2011**, *56*, 4013.

Table 1 – Summary of three imaging modalities; Wide-Field Microscopy, (WFM), Confocal laser scanner microscopy (CLSM) and Digital holographic microscopy (DHM).

Technique	Wide-Field Fluorescence Microscopy (WFM)	Confocal laser scanning microscopy (CLSM)	Digital holographic microscopy (DHM)
Molecular	Yes	Yes	No
Morphology	2D	2D and 3D	2D and 3D
Signal	Fluorescence brightness	Fluorescence brightness	Refractive index
Speed	0.0030 s camera frame rate	1 s	0.0030 s - 0.0006 s
Depth	0.4 to 5.8 µm (60x, NA 0.85 to 20x, NA 0.4) [41]	1 to 100 µm	> 0.1 µm *

* Estimated based on 632 nm laser source with sample of refractive index difference at 0.067. (Please refer to Image and data processing in Experimental section)

Figure 1 – Imaging a developing thrombus.

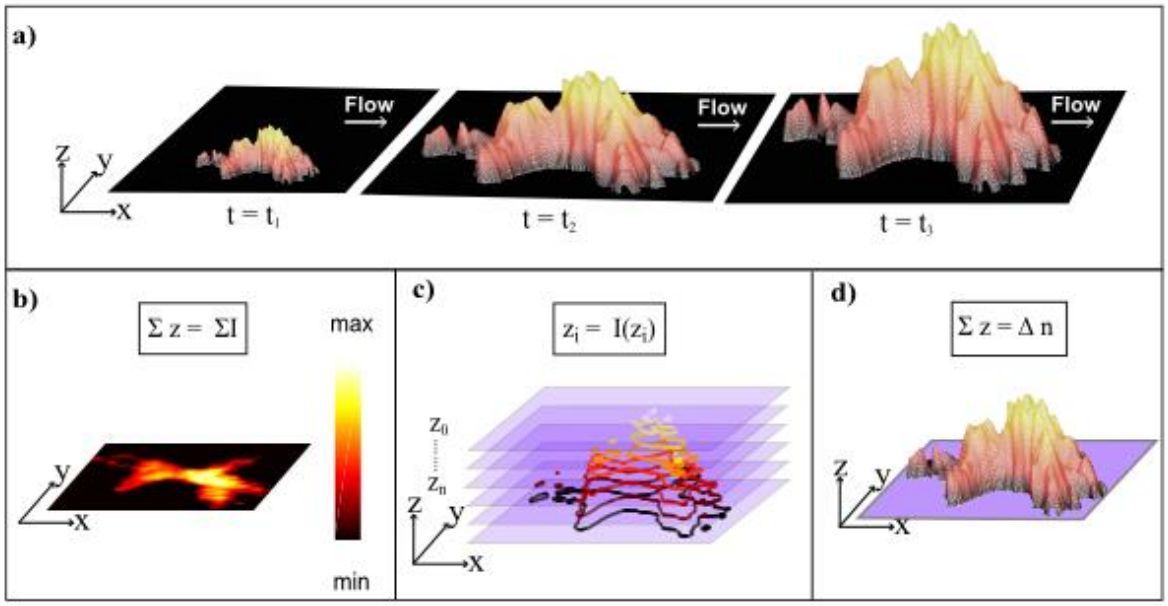

Figure 1. (a) Schematic diagram of a thrombus formed under flow. (b), (c) and (d) Comparison of three imaging techniques, Wide-field fluorescence microscope, Confocal laser scanning microscope and Digital holographic microscopy (DHM) respectively.

Figure 2 – Imaging growth and reduction of thrombus in microfluidic system.

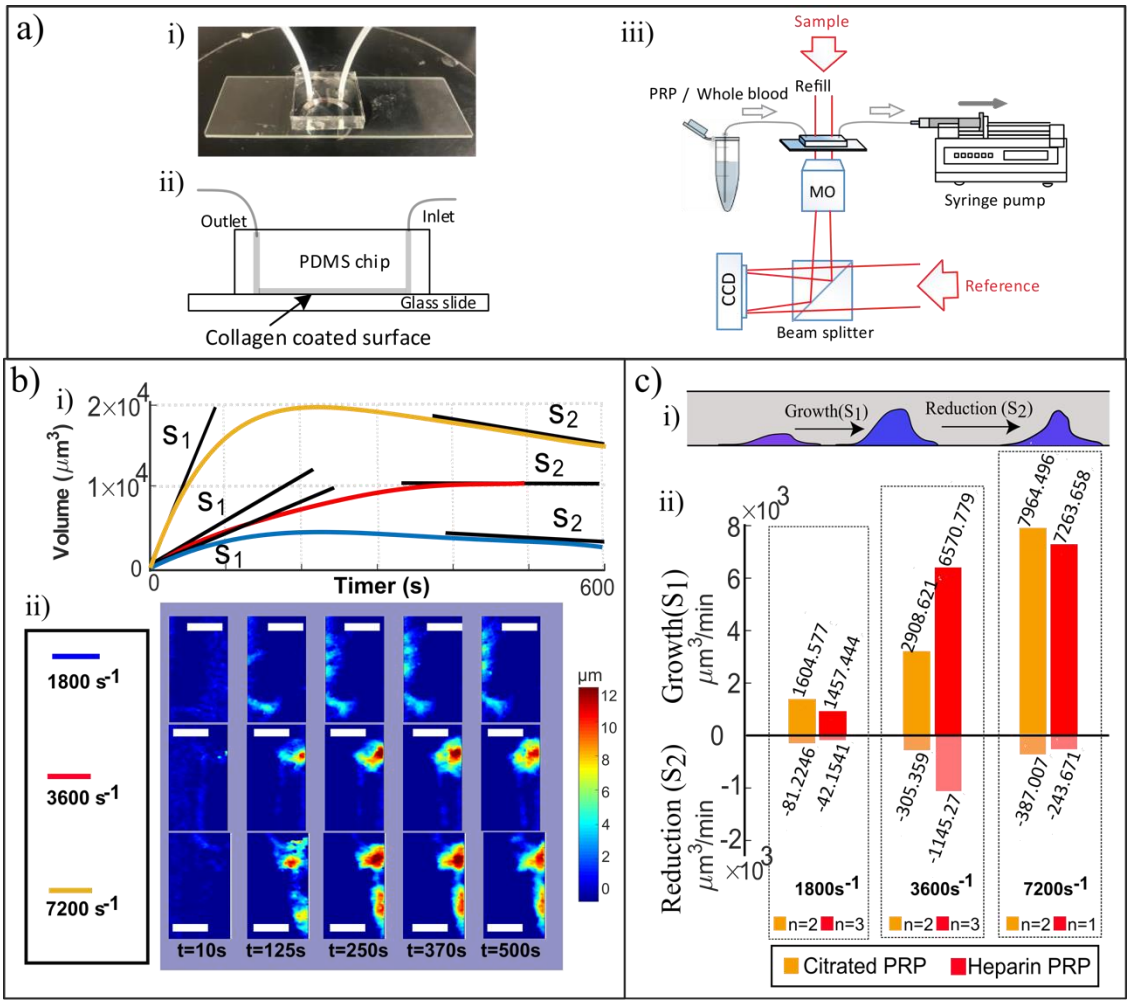

Figure 2. (a), Schematic diagram of experiment setup. (i), picture of polydimethylsiloxane (PDMS) chip used for experiment. (ii), schematic diagram of PDMS microfluidic chip setup. (iii) Platelet Rich Plasma (PRP) and whole blood (heparinized) as sample are perfused over collagen coated PDMS chips. Arrows represent direction of flow. MO is the microscopy objective. The red lines represent the laser light. Figure 2 (b-c). Thrombus formation result and analysis. (b) (i), Example volume growth of three thrombi formed by heparin PRP (from donor 1) under 1800 s^{-1}, 3600 s^{-1} and 7200 s^{-1} shear rates during 10 min perfusion of PRP. The lines in three colours represent three different shear rates. The lines are polynomial fits (with degree of 5 and R-square above 0.98) of smoothed (moving average filter) raw data. The black lines are the linear fit (R-square above 0.9) of the curve lines, representing the speed of the volume accumulations (the front part S1) and volume reduction due to contraction (the end part S2). (b) (ii) The height images show the thrombus forming at different time points. The scale bar is 30 μm and colour bar is in micron. Citrated PRP and whole blood thrombus volume growth curves are located in Supplementary materials. (c) (i) schematic diagram of thrombus formation trend observed in the experiments. (c) (ii) The bar chart of average speed of volume change during thrombus formation. The positive Y axis is the speed of volume accumulation (S1). The negative Y axis is the speed of volume reduction (S2). The heparin PRP sample is indicated by red bars and citrated PRP is indicated by orange bars the size of the sample is indicated below the bar chart.

Figure 3 – Reconstructed multi-view of individual thrombus.

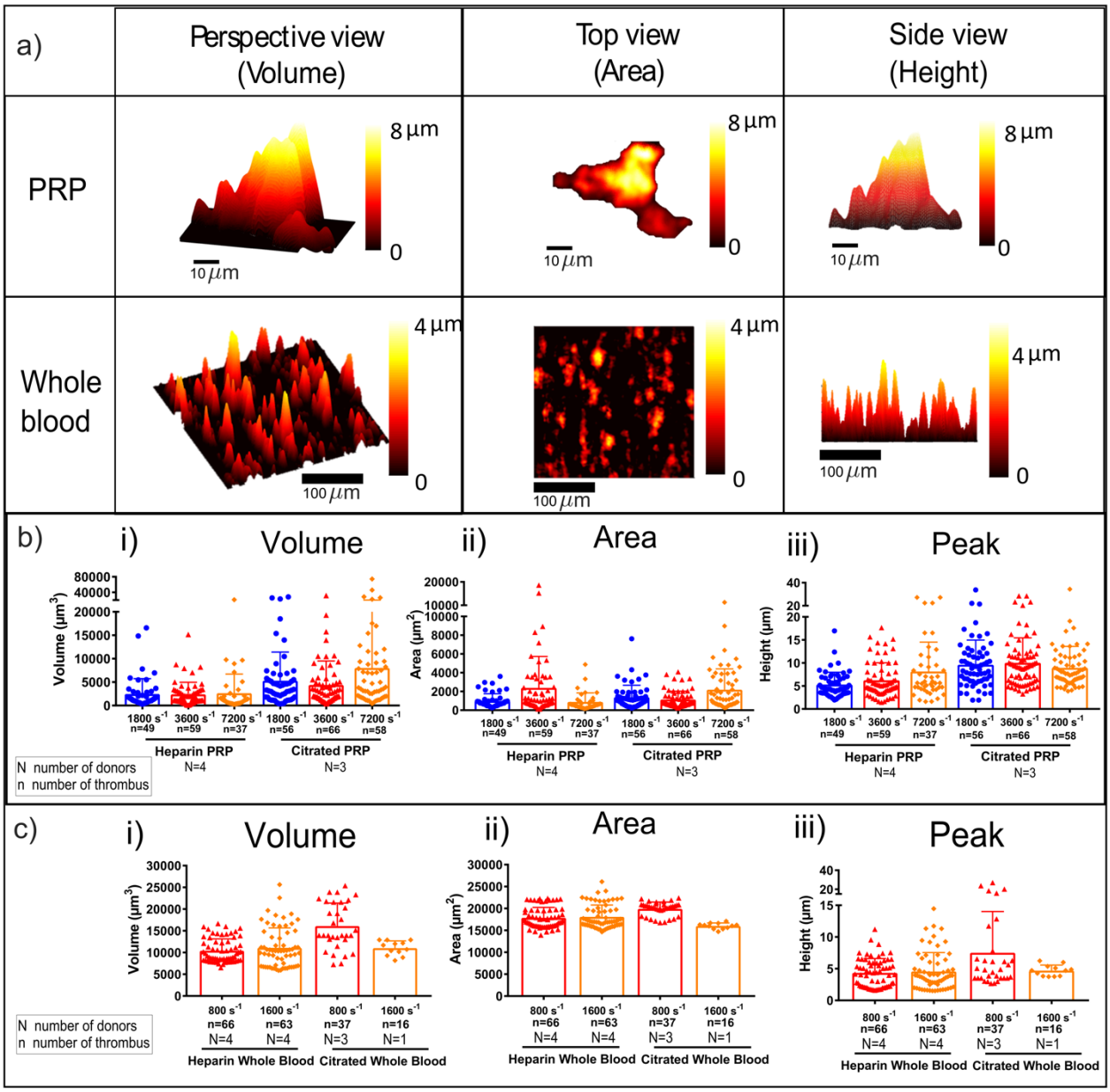

Figure 3. Individual thrombus characteristics. (a) Three columns show the perspective, top and side view of a thrombus formed by PRP and whole blood conditions. The side view is the cross sections of the thrombus through the peak point of it by the direction along with (Y axis) and the direction vertical to (X axis) the PRP and whole blood flow. (b-c) The volume, the surface area and the height of thrombus formed under different shear rates (PRP flow condition: 1800 s^{-1}, 3600 s^{-1}, 7200 s^{-1}; whole blood flow condition: 800 s^{-1}, 1600 s^{-1}; *equivalent shear stress to mid and high PRP shear rates*). The blue circle, red triangle and the yellow diamond are the individual thrombus formed under 1800 s^{-1} PRP flow, 3600 s^{-1} PRP flow (800 s^{-1} whole blood flow), 7200 s^{-1} PRP flow (800 s^{-1} whole blood flow). The number of thrombus is indicated by n beside each bar and the number of donor is indicated by N. Mean shown as +SD.

Figure 4 – Stability of thrombus.

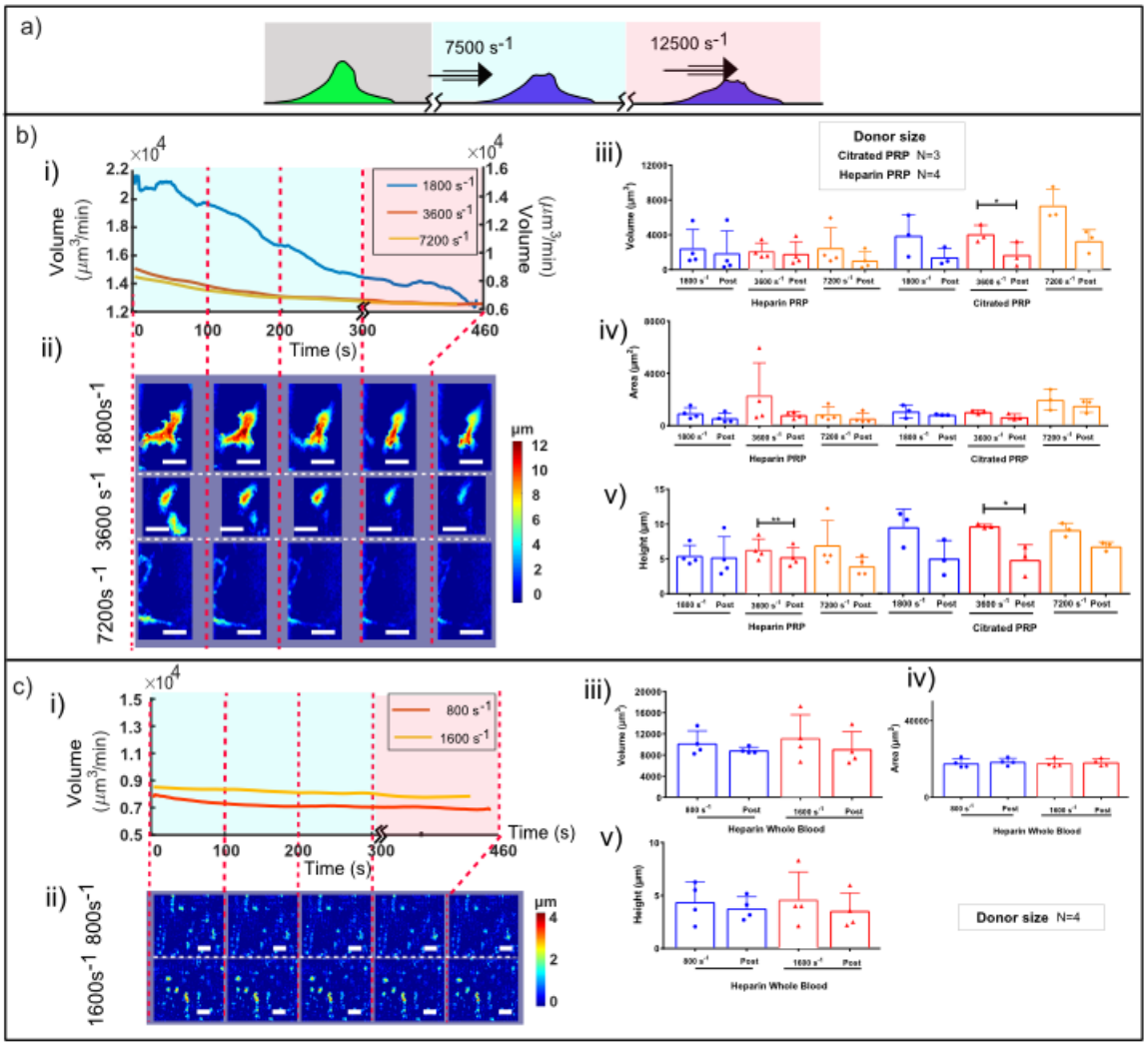

Figure 4. (a) Stability test by exerting high shear rate; buffer flowing at 7500 s^{-1} for 5 min and then 12500 s^{-1} for 2 min) (b) Reduction of thrombus pre-formed by heparin PRP. i) Each line profile traces the thrombus volume that was previously formed under shear rate of 1800 s^{-1} (y-axis left), 3600 s^{-1} (y-axis right) and 7200 s^{-1} (y-axis right) from same donor (d4) respectively. ii) The images below the line plots are the corresponding thrombus at different time points. The scale bar is 40 μm and color bar is in micron. (c iii-v) The bar graphs for average volume, surface area and the peak height data of the thrombus from all donors. Number of thrombus quantified, n> 8 from each donor. The statistical test is a paired t-test, *p<0.05. Mean shown +SD. (c) Reduction of thrombus pre-formed by heparin whole blood flow. i) Each line profile traces the thrombus volume that was previously formed under shear rate of 800 s^{-1} and1600 $s^{-1}$from same donor (d4) respectively. ii) The images below the line plots are the corresponding thrombus at different time points. The scale bar is 40 μm and color bar is in micron. (iii) The statistics bar graph for averaged volume, surface area and the peak data of the thrombus from all donors. Number of thrombus quantified, n> 8 from each donor. The statistical test is a paired t-test. *p<0.05.

Supplementary materials

Supplementary Figures

Figure A1 – distribution of thrombus peak height.

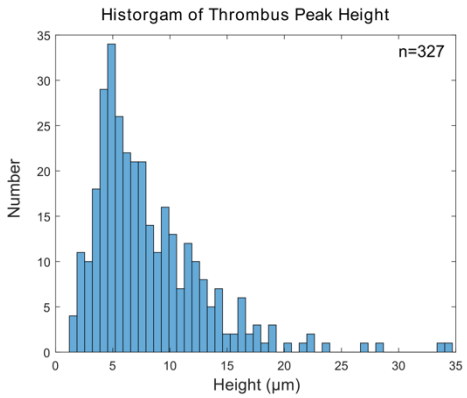

Figure A1. Histogram of thrombus peak height. Thrombus (n=327) were formed by the PRP from all donors (D1, D2, D3, D4 for citrated PRP and d1, d2, d3, d4 for heparin PRP) under all three experimental shear rates.

Figure A2 – Volume profiles for thrombus formation using PRP

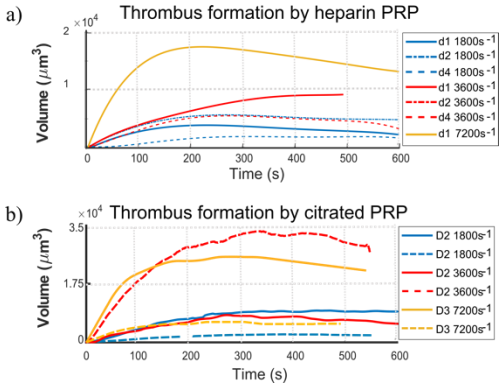

Figure A.2. a) Volume growth of thrombus formed by heparin PRP under three different shear rates. b) Volume growth of thrombus formed by citrated PRP under three different shear rates. Each line stands for each thrombus. The colour of the lines indicates the shear rates of flowing PRP, blue for 1800 s^{-1}, red for 3600 s^{-1} and yellow for 7200 s^{-1}. The type of lines distinguish the thrombus from different donors.

Figure A3 – Stability test of thrombus formed by citrated PRP

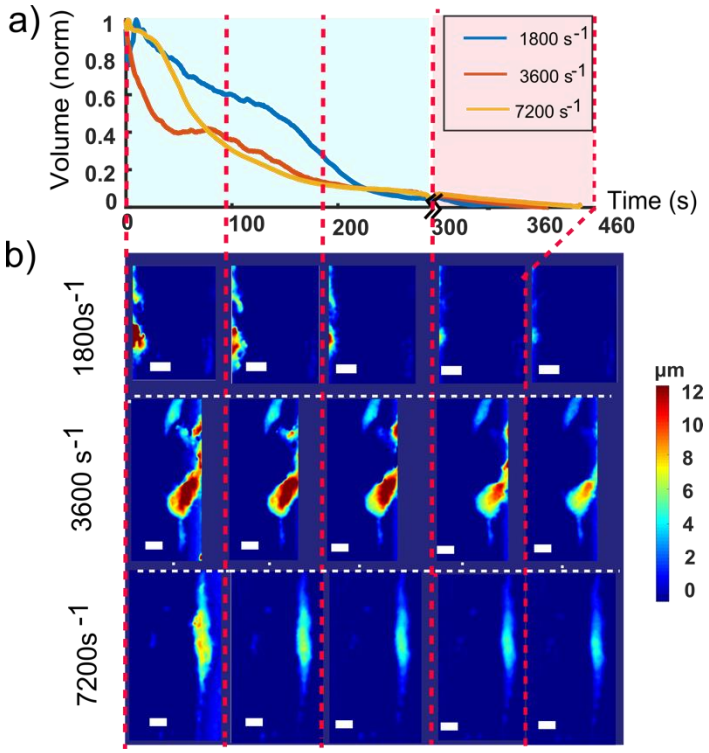

Figure A.3. a) Volume reduction of thrombus formed by citrated PRP during stability test (buffer flowing at 7500 s^{-1} for 5 min and then 12500 s^{-1} for 2 min). Each line profile traces the thrombus volume that was previously formed under shear rate of 1800 s^{-1}, 3600 s^{-1} and 7200 s^{-1} from donor D2 respectively. b) The height map images below the line plots are the corresponding thrombus at different time points. The scale bar is 30 µm and colour bar is in micron.

Figure A4 – Imaging standardization using microspheres

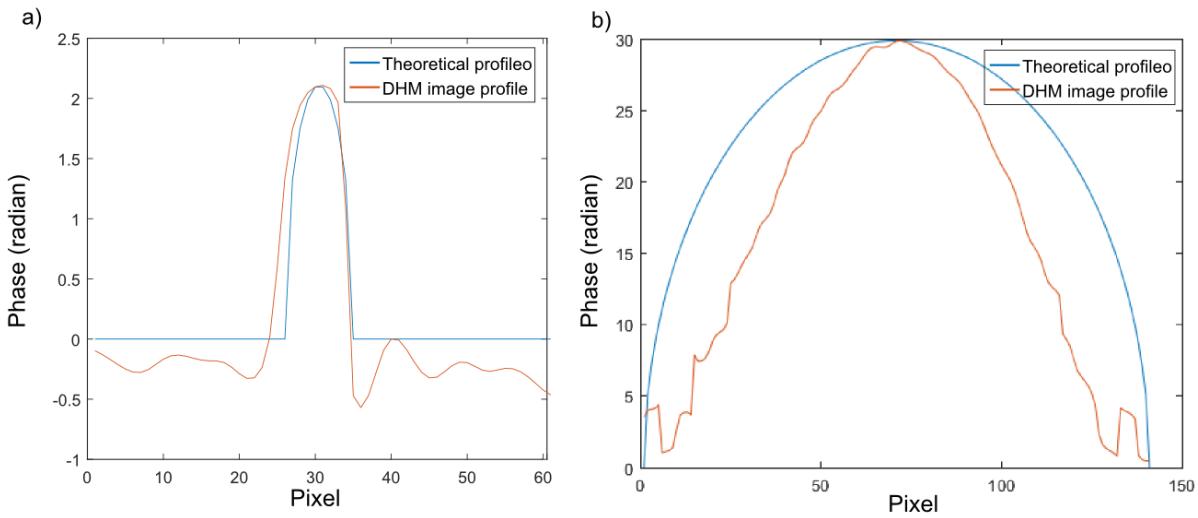

Figure A.4. a) Phase profiles of a 3 µm microsphere. b) Phase profiles of a 3 µm microsphere. The red lines are the reconstructed phase profiles from DHM system. The unit is in radian. The blue lines are the theoretical profiles of the spheres based on the projection of a sphere. The material of the microsphere is polystyrene with refractive index of 1.587.